J|A|C|S
ARTICLES
Published on Web 10/19/2006

Solid-State NMR, Crystallographic, and Computational Investigation of Bisphosphonates and Farnesyl Diphosphate Synthase−Bisphosphonate Complexes

Junhong Mao, Sujoy Mukherjee, Yong Zhang, Rong Cao, John M. Sanders, Yongcheng Song, Yonghui Zhang, Gary A. Meints, Yi Gui Gao, Dushyant Mukkamala, Michael P. Hudock, and Eric Oldfield*

Contribution from the Departments of Chemistry and Biophysics, University of Illinois at Urbana−Champaign, 600 South Mathews Avenue, Urbana, Illinois 61801

Received March 14, 2006; E-mail: eo@chad.scs.uiuc.edu

Abstract: Bisphosphonates are a class of molecules in widespread use in treating bone resorption diseases and are also of interest as immunomodulators and anti-infectives. They function by inhibiting the enzyme farnesyl diphosphate synthase (FPPS), but the details of how these molecules bind are not fully understood. Here, we report the results of a solid-state ^{13}C, ^{15}N, and ^{31}P magic-angle sample spinning (MAS) NMR and quantum chemical investigation of several bisphosphonates, both as pure compounds and when bound to FPPS, to provide information about side-chain and phosphonate backbone protonation states when bound to the enzyme. We then used computational docking methods (with the charges assigned by NMR) to predict how several bisphosphonates bind to FPPS. Finally, we used X-ray crystallography to determine the structures of two potent bisphosphonate inhibitors, finding good agreement with the computational results, opening up the possibility of using the combination of NMR, quantum chemistry and molecular docking to facilitate the design of other, novel prenytransferase inhibitors.

Introduction

Bisphosphonates, such as alendronate (**1**, Fosamax), risedronate (**2**, Actonel), zoledronate (**3**, Zometa), and pamidronate (**4**, Aredia), are an important class of drug molecules that are

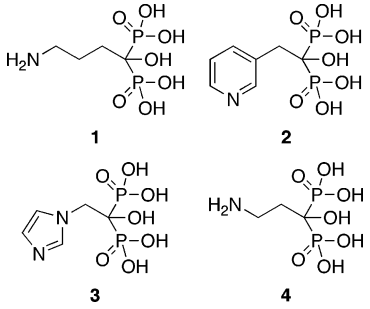

currently used to treat a variety of bone resorption diseases, such as osteoporosis, Paget's disease, and hypercalcemia due to malignancy.[1,2] Bisphosphonates have also been found to stimulate $\gamma\delta$ T cells (containing the Vγ2Vδ2 T cell receptor) of the immune system,[3,4] of interest in the context of cancer immunotherapy,[5−7] plus they have anti-parasitic,[8−11] antibacterial,[12] and herbicidal[13,14] activity. They are potent, low nanomolar inhibitors[13−23] of the enzyme farnesyl diphosphate

(1) Green, J. R. *Oncologist* **2004**, *9*, 3−13.
(2) Reszka, A. A.; Rodan, G. A. *Mini-Rev. Med. Chem.* **2004**, *4*, 711−719.
(3) Das, H.; Wang, L. S.; Kamath, A.; Bukowski, J. F. *Blood* **2001**, *98*, 1616−1618.
(4) Sanders, J. M.; Ghosh, S.; Chan, J. M.; Meints, G.; Wang, H.; Raker, A. M.; Song, Y.; Colantino, A.; Burzynska, A.; Kafarski, P.; Morita, C. T.; Oldfield, E. *J. Med. Chem.* **2004**, *47*, 375−384.
(5) Kato, Y.; Tanaka, Y.; Miyagawa, F.; Yamashita, S.; Minato, N. *J. Immunol.* **2001**, *167*, 5092−5098.
(6) Kunzmann, V.; Bauer, E.; Feurle, J.; Weissinger, F.; Tony, H. P.; Wilhelm, M. *Blood* **2000**, *96*, 384−392.
(7) Wilhelm, M.; Kunzmann, V.; Eckstein, S.; Reimer, P.; Weissinger, F.; Ruediger, T.; Tony, H. P. *Blood* **2003**, *102*, 200−206.
(8) Ghosh, S.; Chan, J. M. W.; Lea, C. R.; Meints, G. A.; Lewis, J. C.; Tovian, Z. S.; Flessner, R. M.; Loftus, T. C.; Bruchhaus, I.; Kendrick, H.; Croft, S. L.; Kemp, R. G.; Kobayashi, S.; Nozaki, T.; Oldfield, E. *J. Med. Chem.* **2004**, *47*, 175−187.
(9) Martin, M. B.; Grimley, J. S.; Lewis, J. C.; Heath, H. T., 3rd; Bailey, B. N.; Kendrick, H.; Yardley, V.; Caldera, A.; Lira, R.; Urbina, J. A.; Moreno, S. N.; Docampo, R.; Croft, S. L.; Oldfield, E. *J. Med. Chem.* **2001**, *44*, 909−916.
(10) Rodriguez, N.; Bailey, B. N.; Martin, M. B.; Oldfield, E.; Urbina, J. A.; Docampo, R. *J. Infect. Dis.* **2002**, *186*, 138−140.
(11) Yardley, V.; Khan, A. A.; Martin, M. B.; Slifer, T. R.; Araujo, F. G.; Moreno, S. N.; Docampo, R.; Croft, S. L.; Oldfield, E. *Antimicrob. Agents Chemother.* **2002**, *46*, 929−931.
(12) Wang, L. S.; Kamath, A.; Das, H.; Li, L.; Bukowski, J. F. *J. Clin. Invest.* **2001**, *108*, 1349−1357.
(13) Cromartie, T. H.; Fisher, K. J. Method of controlling plants by inhibition of farnesyl pyrophosphate synthase. U.S. Patent 5,756,423, May 26, 1998.
(14) Cromartie, T. H.; Fisher, K. J.; Grossman, J. N. *Pestic. Biochem. Physiol.* **1999**, *63*, 114−126.
(15) Bergstrom, J. D.; Bostedor, R. G.; Masarachia, P. J.; Reszka, A. A.; Rodan, G. *Arch. Biochem. Biophys.* **2000**, *373*, 231−241.
(16) Dunford, J. E.; Thompson, K.; Coxon, F. P.; Luckman, S. P.; Hahn, F. M.; Poulter, C. D.; Ebetino, F. H.; Rogers, M. J. *J. Pharmacol. Exp. Ther.* **2001**, *296*, 235−242.
(17) Grove, J. E.; Brown, R. J.; Watts, D. J. *J. Bone Miner. Res.* **2000**, *15*, 971−981.
(18) Keller, R. K.; Fliesler, S. J. *Biochem. Biophys. Res. Commun.* **1999**, *266*, 560−563.
(19) Martin, M. B.; Arnold, W.; Heath, H. T., 3rd; Urbina, J. A.; Oldfield, E., *Biochem. Biophys. Res. Commun.* **1999**, *263*, 754−758.
(20) Montalvetti, A.; Bailey, B. N.; Martin, M. B.; Severin, G. W.; Oldfield, E.; Docampo, R. *J. Biol. Chem.* **2001**, *276*, 33930−33937.
(21) Sanders, J. M.; Gómez, A. O.; Mao, J.; Meints, G. A.; Van Brussel, E. M.; Burzynska, A.; Kafarski, P.; González-Pacanowska, D.; Oldfield, E. *J. Med. Chem.* **2003**, *46*, 5171−5183.

synthase (FPPS, EC 2.5.1.10), which catalyzes the condensation of the isoprenoid dimethylallyl diphosphate (DMAPP, **5**) with isopentenyl diphosphate (IPP, **6**) to form geranyl diphosphate (GPP, **7**), which then condenses with a second IPP molecule to form farnesyl diphosphate (FPP, **8**). As a result, they block

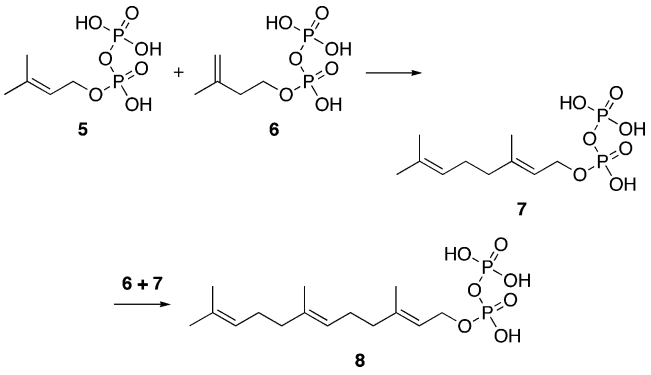

protein prenylation as well as sterol, ubiquinone, dolichol, and heme *a* biosynthesis[1] and, in plants, carotenoid[14] biosynthesis. It has also recently been discovered that treatment of mammalian cells (including osteoclasts) with N-containing bisphosphonates results in the accumulation of the isopentenyl ester of ATP (ApppI),[24] which could also contribute to the efficacy of these drugs in the same way as do the AMP-containing derivatives of clodronate (Bonefos),[25] tiludronate (Skelid), and etidronate (Didronel), by blocking the mitochondrial ADP/ATP transporter.[24, 25] There is, therefore, considerable interest in the use and development of these compounds for treating a broad variety of diseases, and in recent work the X-ray crystallographic structures of alendronate (**1**), risedronate (**2**), and zoledronate (**3**) bound to a variety of FPPS enzymes (from *Staphylococcus aureus*, *Escherichia coli*, and *Homo sapiens*) have been reported,[26−28] as have the structures of alendronate and risedronate bound to *Trypanosoma cruzi* FPPS.[29] In addition to their activity against FPP synthase, some bisphosphonates also inhibit other isoprene biosynthesis pathway enzymes, such as isopentenyl diphosphate/dimethylallyl diphosphate isomerase,[30] geranyl diphosphate synthase,[31] geranylgeranyl diphosphate synthase,[32] squalene synthase,[33] 1-deoxyxylulose-5-phosphate reductoisomerase,[34] and *T. cruzi* hexokinase.[35] In many of these cases, crystallographic structures of bound bisphosphonate inhibitors have not been reported, which complicates their further development. But even in the cases where structures are known, the conformational, tautomeric, and protonation states of the bisphosphonates (and IPP) may not be directly revealed by the protein crystallographic results, necessitating the use of other, complementary techniques sensitive to these parameters.

Another set of questions arise as to the relationship between structure and activity: Is it possible to use information obtained from crystallographic and potentially other (spectroscopic and docking) results to explain activity and, hence, help design novel inhibitors and drugs, including ones which might have, e.g., selective anti-parasitic activity or reduced affinity for bone, of potential interest in cancer therapy?[1] By way of example, consider the four molecules shown below:

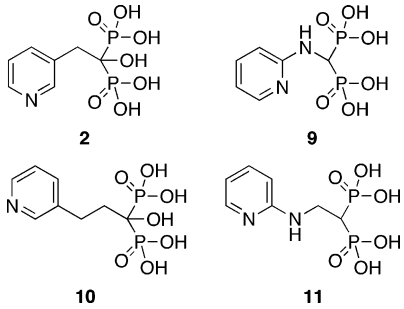

Compound **2** (risedronate) is a potent FPPS inhibitor, as is the 2-aminopyridine, **9**,[21] which has an isoelectronic side chain. However, addition of a single CH_2 group to the side chain of **2** to form homorisedronate (**10**) abrogates virtually all activity,[16,21] but addition of a CH_2 group to **9** to form **11** has no effect on activity. For example, the K_i for **2** is 16 nM, that for **9** is 20 nM (in an expressed *Leishmania major* FPPS[21]), and both **2** and **9** are potent inhibitors of bone resorption in rats.[36] On the other hand, the K_i for homorisedronate (**10**) is 510 nM versus the *L. major* FPPS, and **10** has no effect on inhibiting protein prenylation, is a poor inhibitor of human FPPS, and is ineffective in inhibiting bone resorption (lowest effective dose, LED = 1 mg/kg),[16] whereas **11**, the methylene analogue of **9**, has a K_i = 16 nM in *L. major* FPPS inhibition,[21] an IC_{50} = 2 nM versus an expressed avian FPPS,[37] and an IC_{50} of 40 nM versus human FPPS.[16] The reasons for these differences in activity are far from clear, so the question arises: Can we use information from crystallography and potentially other techniques, such as NMR spectroscopy, to suggest reasons for these differences? While not all the questions raised above about bisphosphonate structure−activity relationships are answered in this work, the combined use of ^{13}C, ^{15}N, and ^{31}P NMR, crystallography, quantum chemistry, and molecular docking does provide important new results about structure−activity relationships for existing

(22) van Beek, E.; Pieterman, E.; Cohen, L.; Löwik, C.; Papapoulos, S. *Biochem. Biophys. Res. Commun.* **1999**, *255*, 491−494.
(23) van Beek, E.; Pieterman, E.; Cohen, L.; Löwik, C.; Papapoulos, S. *Biochem. Biophys. Res. Commun.* **1999**, *264*, 108−111.
(24) Mönkkönen, H.; Auriola, S.; Lehenkari, P.; Kellinsalmi, M.; Hassinen, I. E.; Vepsalainen, J.; Mönkkönen, J. *Br. J. Pharmacol.* **2006**, *147*, 437−445.
(25) Frith, J. C.; Mönkkönen, J.; Blackburn, G. M.; Russell, R. G. G.; Rogers, M. J. *J. Bone Miner. Res.* **1997**, *12*, 1358−1367.
(26) Hosfield, D. J.; Zhang, Y.; Dougan, D. R.; Broun, A.; Tari, L. W.; Swanson, R. V.; Finn, J. *J. Biol. Chem.* **2004**, *279*, 8526−8529.
(27) Kavanagh, K. L.; Guo, K.; Dunford, J. E.; Wu, X.; Knapp, S.; Ebetino, F. H.; Rogers, M. J.; Russell, R. G. R.; Opperman, U. *Proc. Natl. Acad. Sci. U.S.A.* **2006**, *20*, 7829−7834.
(28) Rondeau, J.-M.; Bitsch, F.; Bourgier, E.; Geiser, M.; Hemmig, R.; Kroemer, M.; Lehmann, S.; Rieffel, S.; Strauss, A.; Green, J. R.; Jahnke, W. *ChemMedChem* **2006**, *1*, 267−273.
(29) Gabelli, S. B.; McLellan, J. S.; Montalvetti, A.; Oldfield, E.; Docampo, R.; Amzel, L. M. *Proteins* **2006**, *62*, 80−88.
(30) Thompson, K.; Dunford, J. E.; Ebetino, F. H.; Rogers, M. J. *Biochem. Biophys. Res. Commun.* **2002**, *290*, 869−873.
(31) Burke, C.; Klettke, K.; Croteau, R. *Arch. Biochem. Biophys.* **2004**, *422*, 52−60.
(32) Szabo, C. M.; Matsumura, Y.; Fukura, S.; Martin, M. B.; Sanders, J. M.; Sengupta, S.; Cieslak, J. A.; Loftus, T. C.; Lea, C. R.; Lee, H. J.; Koohang, A.; Coates, R. M.; Sagami, H.; Oldfield, E. *J. Med. Chem.* **2002**, *45*, 2185−2196.
(33) Amin, D.; Cornell, S. A.; Gustafson, S. K.; Needle, S. J.; Ullrich, J. W.; Bilder, G. E.; Perrone, M. H. *J. Lipid Res.* **1992**, *33*, 1657−1663.
(34) Yajima, S.; Hara, K.; Sanders, J. M.; Yin, F.; Ohsawa, K.; Wiesner, J.; Jomaa, H.; Oldfield, E. *J. Am. Chem. Soc.* **2004**, *126*, 10824−10825.
(35) Hudock, M. P.; Sanz-Rodríguez, C. E.; Song, Y.; Chan, J. M. W.; Zhang, Y.; Odeh, S.; Kosztowski, T.; Leon-Rossell, A.; Concepción, J. L.; Yardley, V.; Croft, S. L.; Urbina, J. A.; Oldfield, E. *J. Med. Chem.* **2006**, *49*, 215−223.
(36) Rogers, M. J.; Xiong, X. J.; Brown, R. J.; Watts, D. J.; Russell, R. G. G.; Bayless, A. V.; Ebetino, F. H. *Mol. Pharmacol.* **1995**, *47*, 398−402.
(37) Tarshis, L. Crystal structure of recombinant avian wild type and mutant farnesyl diphosphate synthase and the binding modes of substrate and inhibitor compounds. Ph.D. Thesis, Albert Einstein College of Medicine of Yeshiva University, New York, 1996.

bisphosphonates and can reasonably be expected to facilitate the design of other, novel inhibitors.

Materials and Methods

NMR Spectroscopy. NMR spectra were obtained by using the magic-angle sample spinning technique on one of three spectrometers. The first was a "home-built" system, consisting of an 8.45 T (360 MHz ^{1}H resonance frequency) 3.5 in. bore Oxford Instruments (Oxford, UK) magnet, a Tecmag (Houston, TX) Aries pulse programmer, a variety of other digital and radio frequency circuitries, and a Doty Scientific (Columbia, SC) 5 mm XC5 double-resonance probe. The other two instruments were 600 MHz Infinity Plus spectrometers (Varian, Palo Alto, CA) equipped with 14.1 T, 2.0 and 3.5 in. bore Oxford magnets and Varian/Chemagnetics 3.2 mm T3 HXY probes (used for the protein and ^{15}N NMR experiments). ^{13}C NMR chemical shifts were referenced to the downfield peak of adamantane (taken to be 38.48 ppm from TMS); ^{15}N shifts are reported with respect to a liquid NH_3 standard, taking an external reference of 1 M $^{15}N_2$-urea in DMSO to be at 79.4 ppm downfield from NH_3, as recommended;[38] and ^{31}P NMR chemical shifts were referenced with respect to an external standard of 85% orthophosphoric acid. All shifts use the IUPAC convention that high-frequency, paramagnetic, downfield, or deshielded values are positive.

Synthesis of Labeled Compounds: General Procedure. A mixture of a carboxylic acid (1 mmol), H_3PO_3 (5 mmol), and toluene (4 mL) was heated to 80 °C with stirring. After all solids melted, $POCl_3$ (5 mmol) was slowly added, and the mixture was vigorously stirred at 80 °C for 5 h.[39] Upon cooling of the mixture, the toluene was decanted, and 6 N HCl (3 mL) was added to the residue. The resulting solution was refluxed for 1 h, and then most of the solvent was removed in vacuo. 2-Propanol (25 mL) was added to precipitate a 1-hydroxymethylene bisphosphonate as a white powder, which was filtered, washed with ethanol (5 × 5 mL), dried, and then further purified by recrystallization from H_2O/EtOH.

1-Hydroxy-3-aminopropyl-1,1-bisphosphonic acid-$^{13}C_3$,^{15}N (Pamidronic Acid-$^{13}C_3$,^{15}N). This compound was made from β-alanine-$^{13}C_3$,^{15}N (Cambridge) (250 mg), following the above general procedure (205 mg, 45%).

1-Hydroxy-4-aminobutyl-1,1-bisphosphonic acid-^{15}N (Alendronic Acid-^{15}N). This compound was made from 4-aminobutyric acid-^{15}N (Aldrich) (250 mg), following the above general procedure (210 mg, 47%).

1-Hydroxy-2-(imidazol-1-yl)ethylidene-1,1-bisphosphonic acid-$^{15}N_2$ (Zoledronic Acid-$^{15}N_2$). This compound was made from imidazole-1-acetic acid-$^{15}N_2$, which was prepared according to a published procedure[40] from imidazole-$^{15}N_2$ (Cambridge) (260 mg), following the above general procedure (265 mg, 26%).

1-Hydroxy-2-(pyridin-3-yl)ethylidene-1,1-bisphosphonic acid-^{15}N (Risedronic Acid-^{15}N). 3-Pyridinylacetic acid-^{15}N was prepared according to a published procedure[41] from 3-bromopyridine-^{15}N,[42] followed by hydrolysis (1 N HCl, reflux). Risedronic acid-^{15}N was made from the acid obtained (137 mg) following the above general procedure (185 mg, 65%).

2-(Pyridin-2-ylamino-*2,6*-$^{13}C_2$,$^{15}N_2$)ethylidene-1,1-bisphosphonic Acid. 2-Aminopyridine-*2,6*-$^{13}C_2$,$^{15}N_2$ (200 mg), prepared from KCN-^{13}C,^{15}N (Aldrich) following a published procedure,[43] was reacted with an equivalent amount of tetraethyl vinylidene bisphosphonate[44] in THF at room temperature overnight. Upon purification by column chromatography (silica gel; ethyl acetate/MeOH 20/1), the tetraethyl ester was treated with TMSBr (6 equiv) in acetonitrile for 8 h at room temperature. Upon removal of solvent, the residue was dissolved in EtOH/H_2O (5:1), upon which the product precipitated as a white powder (380 mg, 65%).

Quantum Chemistry. Chemical shielding calculations were carried out by using the Gaussian 98[45] and Gaussian 03[46] programs running on Silicon Graphics (Mountain View, CA) O200, O300, and O2000 computers, typically using four or eight processors. Full experimental details are given in the Supporting Information.

Protein Expression, Purification, and Crystallization for Crystallography and NMR. Protein expression, purification, and crystallization for crystallography was described previously.[47] In brief, *T. brucei* FPPS was expressed and purified as reported earlier and was crystallized at 10 mg mL^{-1} FPPS in 100 mM ammonium acetate, 20% (v/v) 1,2-propanediol, 0.5 mM $MgCl_2$, pH 5.75, in the presence of 5 mols of minodronate (**12**) per mole of FPPS. Crystals formed after several days

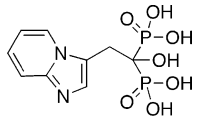

12

and were flash-frozen in liquid nitrogen after addition of 40% (v/v) PEG400 as a cryoprotectant. Basically the same conditions were used for preparing the NMR samples except that a higher PEG level was used, resulting in microcrystalline samples, and both the *T. brucei* and *E. coli*[26] proteins were used.

Bisphosphonate Structures. The structures of the bisphosphonates investigated crystallographically and by NMR (**2**, **11**, and **13**−**20**) are shown in Figure 1 (for convenience, in the protonation states deduced crystallographically). The syntheses of **2**, **11**, **13**, **19**, and **20** have been described elsewhere,[8,9] while **14**−**18** were kindly provided by Novartis Pharma AG (Basel, Switzerland). The X-ray crystallographic structures of **2** and **13** have been reported previously.[48,49] For **11** and **14**−**19**, the compounds were recrystallized from water, and crystals suitable for X-ray structure determination were obtained at pH ∼1. Compound **20** was recrystallized from water by vapor diffusion of ethanol, with two structures, **20a** and **20b**, being obtained at pH values of 6 and 1, respectively.

Small-Molecule Crystallography. Single-crystal data were collected for the pure bisphosphonates on a Siemens (Madison, WI) Platform/CCD diffractometer using the SHELXTL system.[50] Five frame series were filtered for statistical outliers and then corrected for absorption by integration using SHELXTL/XPREP before using SAINT/SADABS to sort, merge, and scale the combined data. Crystal structures were solved by direct methods.[51] Donor H atom positions were refined under restraints to idealized bond distances, with an effective standard deviation of 0.02 Å [$U_{iso} = 1.5U_{eq}$(O,N)]. The remaining H atoms were included as idealized riding contributors [$U_{iso} = 1.2U_{eq}$(C)]. The space group choices were confirmed by successful convergence of the full-

(38) Wishart, D. S.; Bigam, C. G.; Yao, J.; Abildgaard, F.; Dyson, H. J.; Oldfield, E.; Markley, J. L.; Sykes, B. D. *J. Biomol. NMR* **1995**, *6*, 135−140.
(39) Lidor-Hadas, R.; Harel, Z.; Lifshitz-Liron, R.; Kovalevski-Liron, E. Use of certain diluents for making bisphosphonic acids. Patent WO 2003097655, November 27, 2003.
(40) Gil, M. S.; Cruz, F.; Cerdan, S.; Ballesteros, P. *Bioorg. Med. Chem. Lett.* **1992**, *2*, 1717−1722.
(41) Kondo, Y.; Inamoto, K.; Uchiyama, M.; Sakamoto, T. *Chem. Commun.* **2001**, 2704−2705.
(42) Sirimanne, S. R.; Maggio, V. L.; Patterson, D. G. *J. Labeled Compd. Radiopharm.* **1992**, *31*, 163−174.
(43) Lenoir, H. A. C.; Janssen, C. G. M. *J. Labeled Compd. Radiopharm.* **1987**, *24*, 119−123.
(44) Degenhardt, C. R.; Burdsall, D. C. *J. Org. Chem.* **1986**, *51*, 3488−3490.
(45) Frisch, M. J.; et al. *Gaussian 98*, Revision A.7; Gaussian, Inc.: Pittsburgh, PA, 1998.
(46) Frisch, M. J.; et al. *Gaussian 03*, Revision B.03; Gaussian, Inc.: Wallingford, CT, 2004.
(47) Mao, J. H.; Gao, Y. G.; Odeh, S.; Robinson, H.; Montalvetti, A.; Docampo, R.; Oldfield, E. *Acta Crystallogr. Sect. D: Biol. Crystallogr.* **2004**, *60*, 1863−1866.
(48) Gossman, W. L.; Wilson, S. R.; Oldfield, E. *Acta Crystallogr. C* **2003**, *59*, m33−m36.
(49) Szabo, C. M.; Martin, M. B.; Oldfield, E. *J. Med. Chem.* **2002**, *45*, 2894−2903.
(50) *SMART*, Version 5.625; *SAINT*, Version 6.22; and *SHELXTL*, Version 6.12; Bruker AXS Inc.: Madison, WI, 2001.
(51) Sheldrick, G. M. *SHELXL97−2*; University of Göttingen: Göttingen, Germany, 2001.

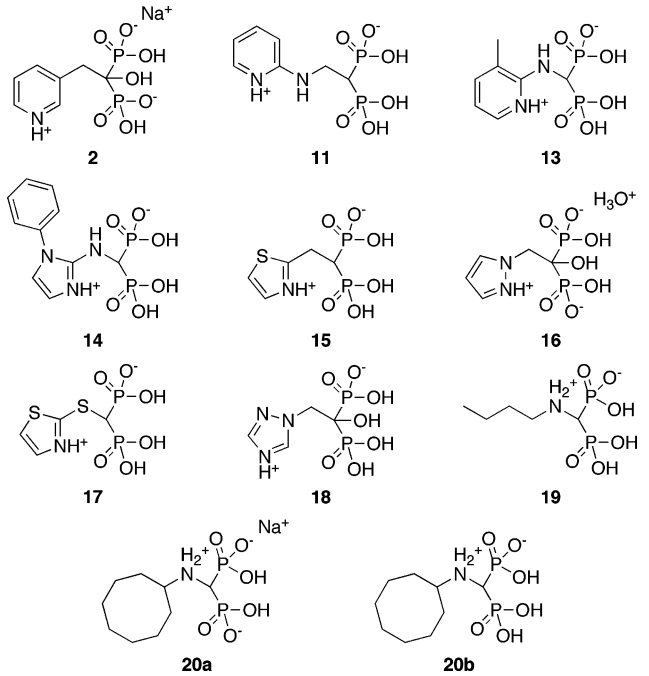

Figure 1. Structures of bisphosphonates investigated. The protonation states shown are those deduced crystallographically.

matrix least-squares refinement on F^2. Final analyses of variance between observed and calculated structure factors showed no dependence on amplitude or resolution. The crystallographic data and structure refinement statistics are summarized in the Supporting Information (Tables S1−S9). Atomic coordinates, bond lengths, angles, and thermal parameters have been deposited with the Cambridge Crystallographic Data Centre (CCDC), deposition numbers 601664−601672.

Protein Crystallography. Diffraction data were obtained at 100 K using an ADSC Q315 CCD detector at the Brookhaven National Synchrotron Light Source beamline X12B (λ = 1.1 Å). The data collection statistics have been reported previously[47] but for convenience are reported again herein. For structure determination, we performed molecular replacement calculations with the program Amore,[52] using as a search model the *T. cruzi* apo-FPPS structure (PDB ID 1YHK[29]) with all solvent molecules and ions removed. Rigid-body refinement was applied to the model obtained. The crystal structure was further refined using X-PLOR[53] and SHELXL-97.[54] Simulated annealing in X-PLOR was carried out to remove model bias. The insertion loop (residues 66−71) in *T. brucei* FPPS, nonidentical residues, and ligands were built and rebuilt with the program *O*[55] using the $2F_o - F_c$ and $F_o - F_c$ electron-density maps. Solvent molecules were included if they had peaks greater than 3σ in the $F_o - F_c$ electron-density map and were within hydrogen-bonding distance of polar protein atoms. Higher hydration shells were filled in the later rounds of refinement if the water peaks were greater than 3σ in the $F_o - F_c$ map and were involved in hydrogen-bonding interactions with neighboring water molecules. The structure was finally refined using SHELXL-97[54] in the resolution range of 30.0−2.5 Å, with a final R_{work}/R_{free} of 24.24/25.98% ($0\sigma(F)$ cutoff). There are two FPPS molecules in an asymmetric unit, with a single minodronate and three Mg^{2+} in each FPPS molecule. Coordinates have been deposited in the Protein Data Bank (PDB ID 2EWG). We then used the same protocols to determine the structure of **11** bound to *T. brucei* FPPS; data collection and refinement statistics are shown in Table S10 in the Supporting Information. Coordinates have been deposited in the Protein Data Bank (PDB ID 2I19).

Docking Calculations. All docking calculations were performed by using the Autodock program[56] with the Lamarckian genetic algorithm implemented therein. Protein structures were taken from the Protein Data Bank[57] (http://www.pdb.org/). For systems in which there was more than one molecule in the unit cell, only the first molecule listed in the PDB file was used in the docking calculations. Active-site phosphate and diphosphate ligands were retained, as were active-site Mg^{2+} and their coordinated water molecules; other non-protein atoms were deleted. For structures with missing protein residues (other than those in the chain termini), the missing residues were added to the X-ray structures and annealed using 500 steepest descent steps through the "minimize subset" command in Sybyl 7.0[58] using Kollman united atom charges, the Tripos force field, essential hydrogens, a default convergence criterion, and a dielectric constant of 80.0. For residues that were missing side-chain atoms, the side chains were repaired and scanned to find geometries that were both consistent with the coordinates of the side-chain atoms that were experimentally observed and sterically allowed by neighboring side chains. Essential hydrogen atoms were added to the proteins using the Biopolymer module in the Sybyl 7.0 program.[58] For phosphonates, diphosphates, and water molecules, Gasteiger charges were applied, with phosphonate groups being treated as fully deprotonated, with resonant oxygen atoms. Magnesium ions were manually assigned charges of 2.0. For the active-site water molecules, the hydrogen atom positions were minimized, keeping all other atoms fixed, to default convergence levels with the Powell minimization algorithm using the Tripos force field and assigned atomic charges. The coordinates of other hydrogen atoms were not adjusted. Further details are given in the Supporting Information.

Results and Discussion

Solid-State ^{13}C and ^{15}N NMR Investigations. The nature of the interactions between a bisphosphonate's side chain and the protein active-site residues is clearly an important question from a structure−activity or drug design perspective. In earlier work,[19] we proposed that bisphosphonates might act as carbocation transition state/reactive intermediate analogues, binding into the allylic (DMAPP) binding site of FPPS, in which case the side chains would most likely be protonated. In the case of risedronate (**2**) binding to the *E. coli* FPPS (a ternary complex with IPP), Hosfield et al.[26] recently reported that the pyridyl side chain of risedronate does, in fact, bind to this hydrophobic pocket and that there is a hydrogen bond between the pyridyl nitrogen and the conserved Thr203. However, since such diffraction methods do not detect H atoms directly, it is not clear whether the pyridyl nitrogen is protonated. Fortunately, however, ^{15}N (and ^{13}C) NMR chemical shifts are very sensitive to protonation state, and this should, in principle, enable the resolution of this question.

We show in Figure 2A−C the ^{15}N MAS NMR spectra of **1** (alendronate), **2** (risedronate), and **13**, and the chemical shifts of these and several other species are shown in Table 1. The shifts of the N-alkylammonium bisphosphonates pamidronate (**4**) and alendronate (**1**) (Figure 2A) are at 34.1 and 37.1 ppm, respectively, essentially the same as for lysine (NH_3^+) residues in amino acids.[59] In risedronate (Figure 2B), the experimental shift in the pure, zwitterionic bisphosphonate is 204.7 ppm, quite characteristic of a protonated or pyridinium-type nitrogen,

(52) Navaza, J. *Acta Crystallogr. A* **1994**, *50*, 157−163.
(53) Brunger, A. T. *X-PLOR*, 3.1; Yale University Press: New Haven, CT, 1992.
(54) Sheldrick, G. M.; Schneider, T. R. *Methods Enzymol.* **1997**, *277*, 319−343.
(55) Jones, T. A.; Zou, J. Y.; Cowan, S. W.; Kjeldgaard, M. *Acta Crystallogr. A* **1991**, *47*, 110−119.
(56) Morris, G. M.; Goodsell, D. S.; Halliday, R. S.; Huey, R.; Hart, W. E.; Belew, R. K.; Olson, A. J. *J. Comput. Chem.* **1998**, *19*, 1639−1662.
(57) Berman, H. M.; Westbrook, J.; Feng, Z.; Gilliland, G.; Bhat, T. N.; Weissig, H.; Shindyalov, I. N.; Bourne, P. E. *Nucleic Acids Res.* **2000**, *28*, 235−242.
(58) *Sybyl*, 7.0; Tripos Inc.: St. Louis, 2004.
(59) Wüthrich, K. *NMR in Biological Research: Peptides and Proteins*; North-Holland Publishing Co.: New York, 1976.

Table 1. ^{15}N NMR Experimental Shifts and Computed Shieldings

	δ^{expt} (ppm)[a]		σ^{calc} (ppm)[b]			δ_{reg}^{pred} (ppm)[c]		
compound	model	protein	Mol	CFP	HB	Mol	CFP	HB
1 (protonated)	37.1	n.d.	252.8	260.2	253.7	38.0	35.5	35.0
1 (neutral)			262.7			29.6		
2 (protonated)	204.7	191.3[d]	83.6	66.5	59.6	181.4	193.0	196.8
2 (neutral)			−107.4			343.2		
3 (protonated)[e]	179.6	178.5[d]	60.8	74.9	82.2	200.7	186.2	177.9
	175.7	170.4[d]	109.2	98.9	80.3	159.7	166.7	179.5
3 (protonated)[e]	179.6	178.5[d]	71.4	80.5	76.1	191.7	181.6	183.0
	175.7	170.4[d]	104.4	98.8	84.5	163.7	166.7	176.0
3 (protonated, model)[f]			63.0			198.8		
3 (protonated, model)[f]			103.4			164.6		
3 (neutral, model)[f]			97.5			169.6		
3 (neutral, model)[f]			−60			303.1		
4 (protonated)	34.1	n.d.	256.1	260.1	255.9	35.2	35.6	33.2
11 (protonated)	n.d.	156.1[g]	131.2	95.0	128.1	141.0	169.8	139.7
	n.d.	97.9[g]	171.2	167.6	166.3	107.1	110.8	107.8
11 (neutral)			−37.2			283.7		
			199.8			82.9		
13 (protonated)	159.0	n.d.	129.2	113.8	113.4	142.7	154.6	151.9
	84.1	n.d.	178.5	204.7	178.2	100.9	80.7	97.9
pyridine	317	n.a.	−97.0	−97.0[h]	−97.0[h]	334.4	325.9[h]	327.3[h]

[a] Experimental shifts are shown for the pure bisphosphonates (model) and for the bisphosphonates bound to FPPS. [b] σ^{calc} values are the predicted shieldings. [c] δ_{reg}^{pred} are predicted shifts obtained using regression equations 1−3. [d] *E. coli* FPPS. [e] Calculations are for two nonequivalent molecules in the unit cell. [f] The model is built by truncating the bisphosphonate and α-carbon moieties in **3** using one of the X-ray crystal structures. [g] *T. brucei* FPPS. [h] Pyridine. n.d. = not determined; n.a. = not applicable.

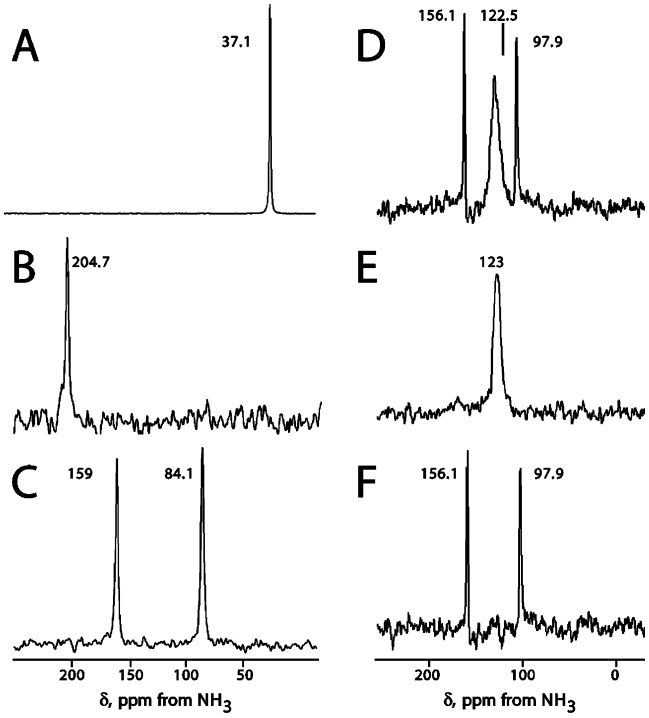

Figure 2. 60 MHz ^{15}N MAS NMR spectra of bisphosphonates: alendronate (A), risedronate (B), **13** (C), $^{15}N_2$-labeled **11** bound to *T. brucei* FPPS (+IPP+Mg^{2+}) (D), and unlabeled FPPS (+Mg^{2+}) (E). (F) Difference spectrum (D − E), showing peaks arising solely from **11**.

whereas the ^{15}N shift for the free base, pyridine, is ∼100 ppm more deshielded, having δ ∼317 ppm.[60] The spectrum of the amidinium **13** contains, as expected, two peaks, having chemical shifts of 159 and 84.1 ppm (from NH_3), which can be attributed to the protonated, amidinium-like nitrogen (at 159 ppm) and the side-chain NH group (at 84.1 ppm), while in zoledronate, the two ^{15}N shifts are at 179.6 and 175.7 ppm (Table 1), as expected for a protonated, imidazolium species.[61] These results give us a benchmark set of chemical shifts, since the protonation states of each compound are known from X-ray crystallography (and the shifts of non-protonated, chemically similar compounds are likewise well known).

We next investigated the ^{15}N NMR chemical shifts of a series of bisphosphonates bound to the *T. brucei* FPPS. A representative spectrum (of ^{15}N-labeled **11** bound to FPPS) is shown in Figure 2D. Two sharp peaks, due to the NH groups in the amidinium form of **11**, can clearly be seen, while the broad central feature arises from the background natural-abundance ^{15}N peptide groups in FPPS, as clearly demonstrated by inspection of the FPPS-only spectrum (Figure 2E) and the difference spectrum (**11** + FPPS, minus FPPS-only, Figure 2F), in which only the two ^{15}N bisphosphonate peaks are visible. The protein shifts (156.1, 97.9 ppm) are clearly those expected for an amidinium (such as **13**). Additional experiments at much longer (up to 50 ms) contact times gave no evidence for the presence of a peak at ∼317 ppm, expected for a non-protonated, 2-aminopyridine,[60] consistent with the idea that **11** binds to FPPS in its protonated or amidinium form. This conclusion is also supported by the results of a ^{13}C NMR investigation of the shifts in $^{13}C_2$,$^{15}N_2$-labeled **11**, in which both the methine (C6) and quaternary (C2) carbon shifts are expected to change significantly on ring protonation. The ^{13}C spectra of **11** bound to the *T. brucei* FPPS are shown in Figure S1 (Supporting Information), with peaks at 152.7 and 138 ppm attributable to C2 (non-protonated) and C6 (methine) carbons, again providing evidence for the presence of only the protonated species, since the free base shifts are expected to occur at ∼150.9 (C6) and ∼166.0 ppm (C2). Similar ^{15}N NMR results and conclusions are obtained for zoledronate (model compound, 179.6/175.7 ppm; bound to FPPS, 178.5/170.4 ppm, Table 1) and for risedronate (model compound, 204.7 ppm; bound to FPPS, 191.3 ppm). In the case of the ^{13}C spectra, both protonated (amidinium) and

(60) Hu, J. Z.; Facelli, J. C.; Alderman, D. W.; Pugmire, R. J.; Grant, D. M. *J. Am. Chem. Soc.* **1998**, *120*, 9863−9869.

(61) Wei, Y. F.; de Dios, A. C.; McDermott, A. E. *J. Am. Chem. Soc.* **1999**, *121*, 10389−10394.

non-protonated (free base) forms of **11** have methine (C6) groups, but there is no peak-splitting due to the presence of two charge states, and the ^{13}C and ^{15}N results are consistent only with the presence of the protonated species in the FPPS active site. Finally, the ^{31}P MAS NMR spectra of these species bound to FPPS exhibit very narrow (~0.6 ppm) lines, consistent with only a single charge-state side chain (spectra discussed below). Clearly, then, these results indicate that all of the potent, nitrogen-containing bisphosphonates bind to FPPS in their fully protonated forms. In the case of alendronate bound to FPPS, we again found a single ^{15}N resonance (data not shown) at $\delta =$ 32.4 ppm, but the shift difference between $-NH_2$ and $-NH_3^+$ groups (~8 pm) is too small to make an unambiguous charge state assignment. However, since the pK_a values of primary amines (pK_a's ~10.6) are ~4−5 pH units larger than those of pyridine or imidazole groups, it seems safe to conclude that, if the less basic species are protonated in the active site, then the more basic species (such as alendronate) will also be protonated.

The ^{15}N chemical shifts seen experimentally in the model compounds are also quite well-predicted from QM calculations. Here, we used single-molecule (Mol), charge field perturbation (CFP) as well as supermolecule hydrogen bonded (HB) cluster calculations to compute the ^{15}N NMR chemical shieldings, together with an evaluation of the ^{15}N NMR shift/shielding of pyridine (fully optimized with B3LYP/6-311G**) as a reference. Results are shown in Table 1. From comparison with the experimental chemical shifts, we obtain the following fitting equations:

$$\delta^{pred}(\text{Mol}) = (297.6 - \sigma^{calc})/1.18 \quad (1)$$

$$\delta^{pred}(\text{CFP}) = (303.9 - \sigma^{calc})/1.23 \quad (2)$$

$$\delta^{pred}(\text{HB}) = (295.7 - \sigma^{calc})/1.20 \quad (3)$$

with $R^2 = 0.961$, 0.988, and 0.988 and rmsd errors between theory and experiment of 19.4, 11.1, and 10.8 ppm (6.9%, 3.9%, and 3.8% of the 282.9 ppm shift range seen experimentally) for single-molecule (Mol), CFP, and supermolecule calculations, respectively. Both CFP and supermolecule calculations improve the shift predictions, indicating the importance of intermolecular contributions to ^{15}N NMR shielding. The best results, obtained by using the hydrogen-bond partner model, are shown in Figure 3. Nevertheless, even single-molecule calculations have a reasonable correlation ($R^2 = 0.961$, 6.9% error), and, as shown in Figure 3 (in red), shielding calculations based on the "wrong" protonation states are readily identified. For alendronate (**1**), risedronate (**2**), zoledronate (**3**), and **11** (bound to FPPS), as shown in Table 1, the experimental shifts found are close to those seen in the corresponding pure or model compounds, all of which contain protonated side chains. With alendronate, the predicted (single-molecule) shift differences between the protonated and non-protonated (NH_3, NH_4^+) species are relatively small (~8 ppm, Table 1), but with risedronate (**2**), zoledronate (**3**), and **11**, there are major shift differences predicted theoretically (~140−160 ppm), with only the shifts of the protonated form being close to those seen experimentally in proteins.

Solid-State ^{31}P NMR Investigations. The results discussed above show that ^{15}N (and ^{13}C) NMR techniques can be used to deduce bisphosphonate side-chain charges in proteins and that QM methods can predict ^{15}N shifts (at least in model compounds). The next question of interest is to what extent can ^{31}P NMR shifts be predicted in these bisphosphonates, both in model systems and in proteins, where questions as to charge state are of importance in molecular docking, drug design, and even drug delivery (bone adsorption) applications?

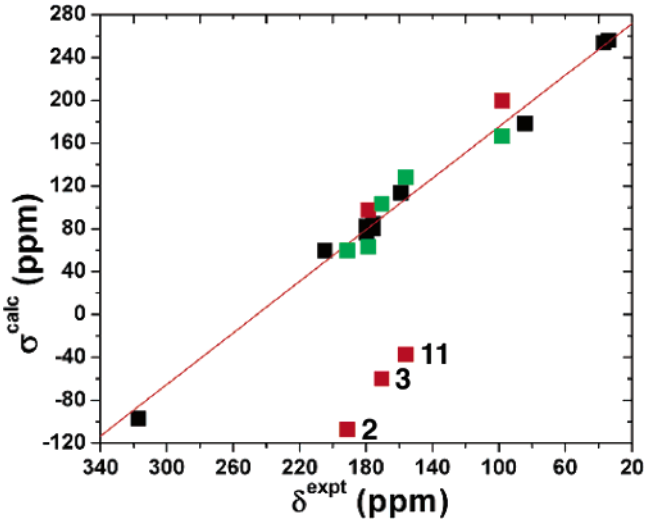

Figure 3. ^{15}N NMR experimental chemical shifts versus computed shieldings for bisphosphonates from supermolecule calculations. The red symbols correspond to shifts for (putative) non-protonated species, and green symbols are for protonated species.

To date, there have been two QM studies reported of the NMR chemical shift/shielding tensors in phosphates[62,63] and one methodological study of three bisphosphonates.[64] Here, we extend these studies to a much larger range of bisphosphonates to determine to what extent QM methods can be used to predict ^{31}P shifts in a variety of bisphosphonates, and then we use these methods to investigate ^{31}P NMR shifts for a bisphosphonate as well as a diphosphate (IPP) bound to a protein, where structures are less certain. To begin with, we determined the X-ray crystallographic structures of nine bisphosphonates: **11**, **14**−**19**, and **20a**,**b** (two structures). These structures are shown as ORTEP diagrams in Figure 4. In all cases except two (**16**, **20a**), the molecules crystallized in their zwitterionic forms and contained, therefore, one neutral ($P(O)(OH)_2$) and one anionic ($P(O)(O^-)(OH)$) phosphonate group (Figure 4). In the case of **16**, the H_3O^+-containing, dianionic species formed, while in the case of **20a**, an Na^+-containing species formed. All side chains were found to be protonated, consistent with the strong basicity of the side chains in **11**, **14**, **19**, and **20** and the acidic conditions required to obtain diffraction-quality crystals of the significantly less basic species, **15**−**18**. In all of the new structures (except **19**), there is only one molecule in the asymmetric unit, resulting in the general case in two chemically shifted ^{31}P NMR peaks, one from each phosphonate group. In the case of **19**, the two molecules in the asymmetric unit are clearly nonequivalent, an effect which might complicate data analysis since up to four ^{31}P NMR peaks might be anticipated. Upon inspection of all model compound crystallographic P−O bond lengths, it can be seen that there is clearly a bimodal distribution (Figure S2A in the Supporting Information, shown in black), with P−O bonds in which the O atom is not protonated (i.e., P═O or P−O^-) occurring in the range ~1.48−1.53 Å, while in the case of

(62) Alam, T. M. *Int. J. Mol. Sci.* **2002**, *3*, 888−906.
(63) Potrzebowski, M. J.; Assfeld, X.; Ganicz, K.; Olejniczak, S.; Cartier, A.; Gardiennet, C.; Tekely, P. *J. Am. Chem. Soc.* **2003**, *125*, 4223−4232.
(64) Zhang, Y.; Oldfield, E. *J. Phys. Chem. B* **2004**, *108*, 19533−19540.

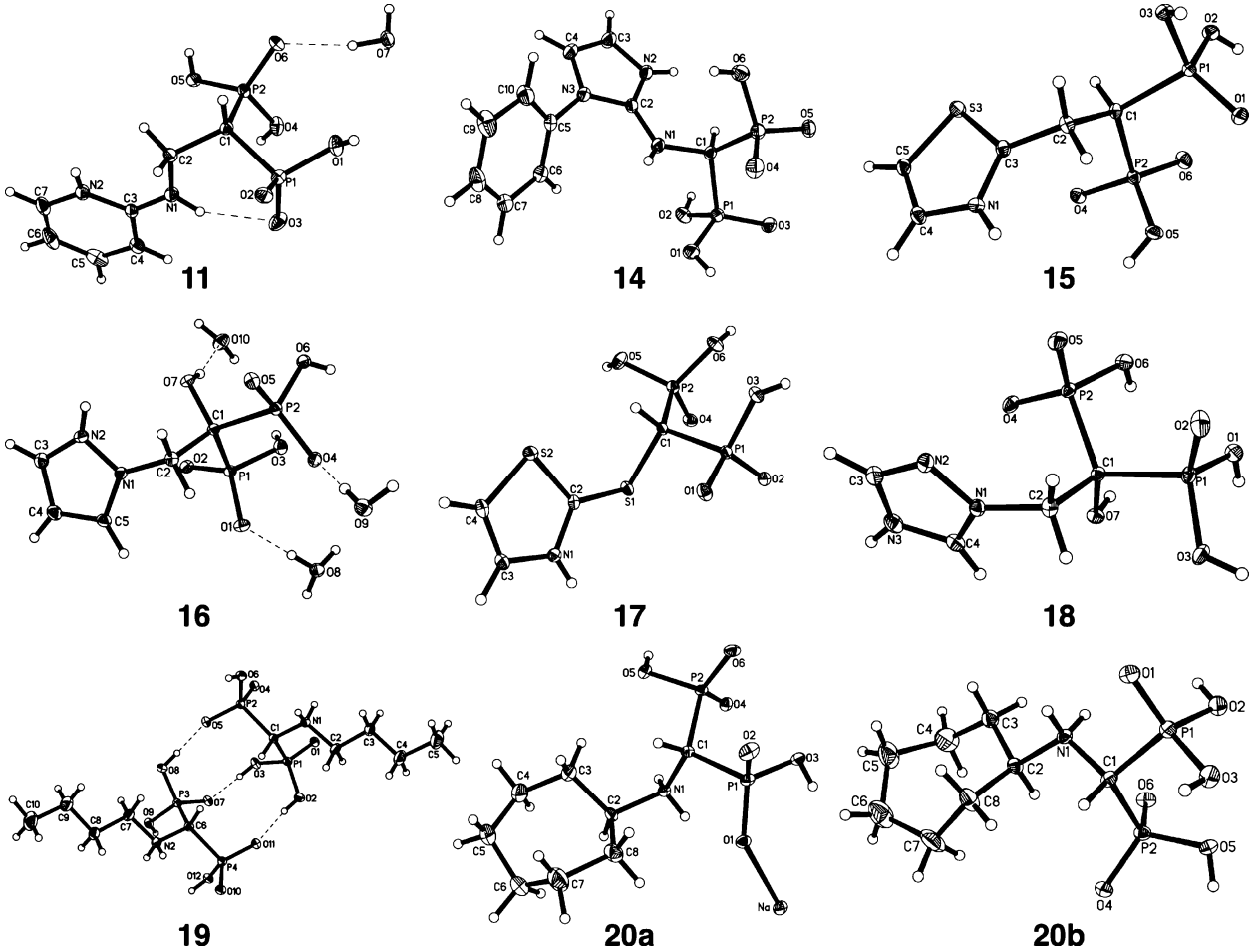

Figure 4. Single-crystal X-ray structures of compounds **11** and **14**−**20**. Displacement ellipsoids are drawn at the 35% probability level, and H atoms are shown as small spheres of arbitrary radii. Five water molecules in **14** and a disordered structure with low occupancy in **20a** are omitted for clarity. Detailed structural information is provided in the Supporting Information.

protonated P−O groups (i.e. P−O−H), this distance increases and is in the range 1.52−1.60 Å, consistent with more limited results reported earlier.[48] The lack of narrow clusters of P═O (double bond) and P−O$^-$ (single bond) distances clearly indicates the importance of resonance effects, and indeed the P═O and P−O$^-$ bond lengths are, in most cases, virtually identical in each of the systems investigated. In proteins, however, there appears to be a larger range of bisphosphonate P−O bond lengths (shown in Figure S2B in the Supporting Information). However, use of these bond lengths in NMR chemical shift calculations does not enable accurate shift predictions (discussed below), since such lengths are expected to depend very strongly on the standard distance and force constants used in the refinement.

We next investigated the solid-state ^{31}P NMR spectra of crystalline samples of **2**, **11**, **13**, **14**, and **16**−**20a**. Compound **15** was not investigated, due to the difficulty in obtaining sufficient crystals. Figure S3 (Supporting Information) shows representative ^{31}P MAS NMR spectra of **18** (Figure S3A, a single peak), **13** (Figure S3B, two isotropic peaks), and **19** (Figure S3C, four isotropic peaks). For comparison, in Figure S3D we show the solution ^{31}P NMR spectrum of **19**, which exhibits only a single peak, due to chemical exchange shift averaging effects in solution. These results are of interest since they show that there can be a wide range of chemical shifts in bisphosphonates, plus there are some surprising observations. For example, with the triazole **18**, the crystal structure clearly reveals one neutral and one anionic phosphonate group, but the MAS NMR spectrum shows only one peak—is this effect predictable using quantum chemistry? In the case of **19**, however, there are four peaks seen in the MAS NMR spectrum. With our solution of the crystallographic structure of **19**, this effect can be appreciated—at least qualitatively, since there are two molecules in the asymmetric unit—but this adds to the complexity of the spectral assignment question and, hence, the quantum chemical analysis. To help with the assignment question with **19**, we thus carried out a series of 2D ^{31}P−^{31}P RFDR[65] experiments, in order to make connectivities between the neutral and anionic phosphonate groups in each of the two molecules in the unit cell. As may be seen in Figure S3E, at the short mix time of 25 ms, peak **a** is connected to peak **c**, while peak **b** is connected to peak **d**, reflecting the short-range (3.0 Å) intramolecular connectivities, while at the larger mix time of 100 ms, the intermolecular (P−P distances of ∼4.6 Å) cross-peaks are also clearly visible (Figure S3F). These results enable pairing of the four peaks observed, facilitating their use in analysis of the shielding calculation results.

In addition to these isotropic chemical shift measurements, we determined the MAS NMR spectra of **2**, **11**, **13**, **14**, and **16**−**20a** at spinning speeds of 3000, 3500, 4000, 4500, and in

(65) Griffiths, J. M.; Griffin, R. G. *Anal. Chim. Acta* **1993**, *283*, 1081−1101.

Table 2. Experimental ^{31}P Solid-State NMR Chemical Shift and Shift Tensor Elements, and Computed Chemical Shieldings and Shielding Tensor Elements for Bisphosphonates

		experimental δ (ppm)[a]				computed σ (ppm)[b]				predicted δ_{reg}^{pred} (ppm)[c]			
compound	site	δ_i	δ_{11}	δ_{22}	δ_{33}	σ_i	σ_{11}	σ_{22}	σ_{33}	δ_i	δ_{11}	δ_{22}	δ_{33}
2	PO_3H^-	18.9	90.7	15.0	−49.0	336.4	251.3	337.0	420.7	18.7	82.2	17.3	−46.1
	PO_3H^-	17.0	85.4	14.2	−48.6	340.2	255.5	335.4	429.7	14.6	79.0	18.5	−53.0
11	PO_3H_2	23.3	70.8	35.7	−36.5	328.3	265.5	286.4	433.1	27.4	71.4	55.6	−55.5
	PO_3H^-	19.0	79.2	13.2	−35.5	333.8	258.5	318.2	424.6	21.5	76.7	31.5	−49.1
13	PO_3H_2	9.2	73.2	19.2	−64.7	344.3	287.2	315.6	430.1	10.2	55.0	33.5	−53.3
	PO_3H^-	14.6	84	8.4	−48.6	340.1	258.0	339.8	422.6	14.7	77.1	15.2	−47.6
14	PO_3H_2	13.2	70.7	1.8	−32.8	340.9	273.1	318.2	431.3	13.9	65.7	31.5	−54.2
	PO_3H^-	10.2	88.3	13.7	−71.3	346.9	254.4	347.4	438.9	7.4	79.8	9.4	−59.9
16	PO_3H^-	16.3	84.1	13.0	−48.3	337.4	266.5	337.2	408.6	17.6	70.7	17.1	−37.0
	PO_3H^-	14.6	82.5	6.8	−45.5	341.1	257.4	341.8	424.0	13.7	77.6	13.6	−48.6
17	PO_3H_2	18.0	75.3	8.1	−29.4	334.1	290.6	302.3	409.3	21.2	52.4	43.6	−37.5
	PO_3H^-	15.0	83.8	6.2	−45.2	340.1	254.9	335.8	429.7	14.7	79.5	18.2	−53.0
18	PO_3H_2	12.9	77.3	11.9	−51.7	341.5	272.2	311.4	441.0	13.2	66.4	36.7	−61.5
	PO_3H^-	12.9	77.3	11.9	−51.7	343.7	249.5	333.4	448.1	10.9	83.6	20.0	−66.9
19	PO_3H_2	9.8	80.8	26.9	−78.3	347.5	271.4	315.0	456.0	6.8	67.0	33.9	−72.9
	PO_3H^-	−2.3	83.0	−5.5	−84.3	353.1	256.7	343.7	458.9	0.8	78.1	12.2	−75.1
	PO_3H_2	12.6	77.1	0.2	−39.6	338.2	276.0	319.5	419.1	16.8	63.5	30.5	−44.9
	PO_3H^-	0.5	86.6	7.9	−93.0	351.5	251.3	337.1	466.2	2.5	82.2	17.2	−80.6
20a	PO_3H^-	8.9	85.0	1.8	−60.2	345.4	253.1	330.5	452.6	9.0	80.8	22.2	−70.3
	PO_3H^-	7.7	83.6	4.3	−64.8	347.0	244.8	327.3	468.8	7.3	87.1	24.6	−82.6

[a] Experimental shifts and shift tensor elements, in ppm from 85% H_3PO_4. [b] Computed shieldings. [c] Predicted chemical shifts and shift tensor elements obtained by using the regression equations in the text (eqs 4 and 5).

some cases at 5000 (±1) Hz and then used the Herzfeld−Berger method[66] as embodied in the HBA program[67] to deduce δ_{11}, δ_{22}, and δ_{33}, the principal components of the chemical shift tensor. The experimental isotropic chemical shifts and shift tensor elements so derived for each compound are given in Table 2. Using the known crystal structures, we next computed the ^{31}P NMR chemical shielding tensor elements for each molecule investigated, using the HF method with a 6-311++G(2d,2p) basis and a 7.5 Å radius Merz−Kollman charge lattice. Results are shown in Table 2 and Figure 5. We also investigated the effects of omitting charge field perturbation (CFP) and the use of the DFT B3LYP method (with and without CFP), but the results showed no improvement. The overall correlation between the computed isotropic chemical shieldings (σ_i) and the experimental chemical shifts (δ_i), as well as the computed shielding tensor elements (σ_{ii}) and the experimental shift tensor elements (δ_{ii}), is good, as can be seen in panels A and B of Figure 5, respectively. For the nine compounds (20 sites) investigated, we find an R^2 value of 0.890 and a standard deviation of 2.1 ppm over the entire 26 ppm range in δ_i, or about an 8% error (the standard deviation divided by the range). To the isotropic shielding results obtained in this paper (shown as ■ in Figure 5A), we can also add those obtained for a variety of other phosphonates,[64] shown as □ in Figure 5A, which then yields an R^2 of 0.922 and a standard deviation of 2.1 ppm, corresponding to about a 6% error over the entire 35 ppm experimental chemical shift range. The slope is also good (0.93), although, as expected, there are deficiencies in the absolute shielding, which we find from the regression line,

$$\delta_{iso}^{pred} = (353.8 - \sigma_{iso}^{calc})/0.93 \quad (4)$$

the absolute shielding (of 85% H_3PO_4) being 353.8 ppm, versus the 328.35 ppm value reported by Jameson et al.[68] For the shift/shielding tensor component correlation (Figure 5B), we again find a good correlation: $R^2 = 0.944$ for the 20 sites investigated,

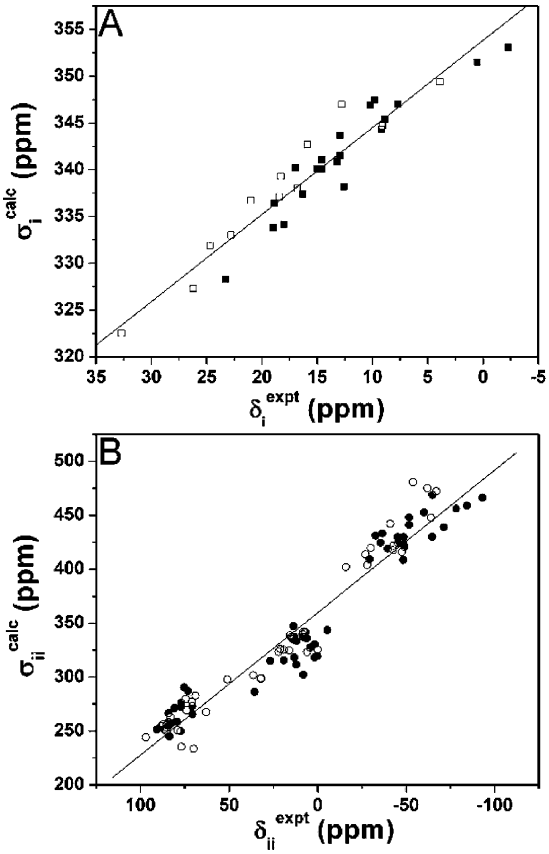

Figure 5. Experimental and HF/MK charge lattice computational results for ^{31}P NMR properties. (A) Experimental isotropic chemical shifts vs calculated chemical shielding. (B) Experimental chemical shift tensor elements vs calculated chemical shielding tensor elements. The solid symbols are for the sites studied in this work; the open symbols are from a previous study (ref 64).

(66) Herzfeld, J.; Berger, A. E. *J. Chem. Phys.* **1980**, *73*, 6021−6030.
(67) Eichele, K.; Wasylishen, R. *HBA*, 1.4; Dalhousie University: Halifax, Canada, 2001.
(68) Jameson, C. J.; de Dios, A.; Jameson, A. K. *Chem. Phys. Lett.* **1990**, *167*, 575−582.

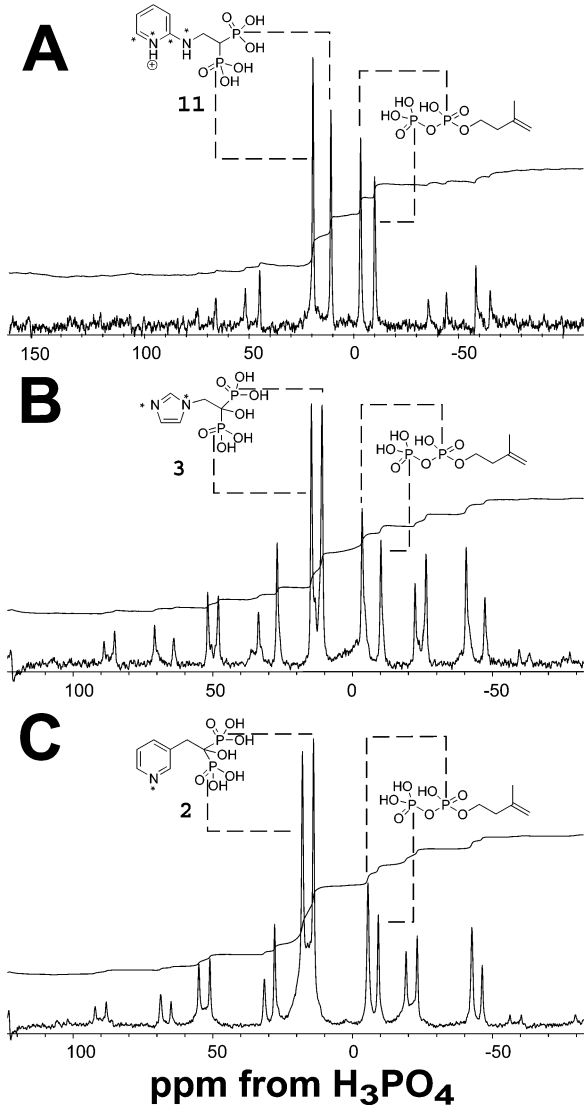

Figure 6. 242 MHz ^{31}P NMR spectra of bisphosphonates bound to FPPS (+Mg^{2+}+IPP): (A) *T. brucei* FPPS + **11**, (B) *T. brucei* FPPS + zoledronate (**3**), and (C) *E. coli* FPPS + risedronate (**2**).

with a slope of 1.26. With the addition of the results for other, simple phosphonates (○ in Figure 5B), we obtain $R^2 = 0.941$ and the following equation relating the predicted shift tensor elements with those computed theoretically:

$$\delta_{ii}^{pred} = (359.8 - \sigma_{ii}^{calc})/1.32 \quad (5)$$

Clearly, there are some fortuitous error cancellations in the δ_i predictions, since the slope of the δ_{ii}/σ_{ii} correlation is worse than that found for δ_i, although of course the very good R^2 and rms errors found (about 7% of the range seen experimentally) do enable good predictions of the experimental results.

^{31}P MAS NMR of Bisphosphonates and IPP Bound to FPPS. We next investigated the binding of **11**, zoledronate (**3**), and risedronate (**2**) to FPPS using ^{31}P NMR to try to provide information on the protonation states of the bisphosphonate and diphosphate side chains, which might be of use in docking investigations. We investigated the ternary complexes containing IPP (+ three Mg^{2+}), and representative spectra are shown in Figure 6A−C. In all cases, there are four isotropic peaks having narrow (0.6 ppm) line widths, together with a series of spinning sidebands. At the short (2 s) recycle times used to record most spectra, the integrated bisphosphonate:IPP peak areas were ∼1.3:1, but at a long (10 s) recycle time, the peak area ratio for **11**:IPP was 1.1(±0.1):1, consistent with the expected 1:1 bisphosphonate:IPP binding stoichiometry in these ternary (bisphosphonate:IPP:Mg^{2+}) complexes. In the case of IPP binding to the *T. brucei* protein, the IPP isotropic shifts in the presence of **11**, zoledronate (**3**), and risedronate (**2**) are virtually identical: −3.6/−3.4/−3.5 and −10.2/−10.2/−10.2 ppm, while in the case of risedronate bound to the *E. coli* protein, the IPP shifts are −5.5 and −9.2 ppm, indicating small differences in packing. The shifts of risedronate bound to both the *T. brucei* and *E. coli* proteins are also almost identical, 18.0 versus 17.9 and 14.0 versus 13.9 ppm (Table 3), indicating that both the IPP and bisphosphonate (DMAPP) binding-site structures are highly conserved. The bisphosphonate ^{31}P NMR chemical shifts seen in all cases are, however, more shielded than those observed in the model compounds. This might reasonably be thought to arise from the presence of more anionic species than those investigated in the well-characterized model systems, due to binding to the three Mg^{2+} ions in the active site. This general increase in shielding is also seen to some extent in model systems containing monovalent cations. For example, in the zwitterionic form of risedronate there are two ^{31}P NMR peaks, having chemical shifts of 22.8 and 16.8 ppm[64] downfield from 85% H_3PO_4 (Table 3), corresponding to the protonated (−$PO(OH)_2$) and monoanionic phosphonates (−$PO(OH)(O^-)$), respectively. But in the monosodium salt, the shifts are at 18.9 and 17.0 ppm (Table 2), corresponding to partial ionization of the fully protonated species (a 4.2 ppm increase in shielding, due to ionization).

On the basis of these observations, we next carried out a series of ^{31}P NMR shielding calculations for risedronate bound to the *E. coli* FPPS protein. The initial results obtained were poor (>40 ppm errors in isotropic shifts) for both the risedronate ligand alone or risedronate in a supermolecule cluster (extracted from the protein X-ray structure, PDB ID 1RQJ) (Table 3). These results improved considerably when we carried out a geometry optimization on the supermolecule cluster shown in Figure S4 of the Supporting Information (coordinates provided in Table S11), where we found shifts of 17.2 and 15.2 ppm, to be compared with the 17.9 and 13.9 ppm results found experimentally. The principal cause of the variations in predicted shifts when using the different structures is likely due to the larger range in bond lengths seen in the protein structures, as illustrated in Figure S2B, which become much more uniform (Figure S2A, green symbols) as well as closer to those seen in model compounds upon geometry optimization. In these calculations, we used fully deprotonated bisphosphonate groups, based on our inspection of the binding geometry seen experimentally, in which the phosphonate groups are close to either two or three Mg^{2+}. To verify the conclusion about the protonation state, we also attempted a series of QM calculations on a monoprotonated bisphosphonate; however, there were large geometry changes on optimization, inconsistent with the X-ray structure, which we believe rules out this binding motif.

In addition to the bisphosphonate ^{31}P NMR chemical shifts, we also obtained the experimental ^{31}P NMR chemical shifts of the IPP substrate bound to FPPS. The shifts seen (∼ −4 to −5 ppm and ∼ −9 to −10 ppm) are basically those seen for IPP in

Table 3. Experimental and Predicted ^{31}P NMR Shifts in FPPS−Bisphosphonate−IPP Complexes[a]

molecule		system	FPPS	structure	δ(P1)[b] (ppm)	δ(P2)[b] (ppm)	δ_{av}[c] (ppm)	$\lvert\Delta\delta\rvert$[c] (ppm)	E[d] (kcal/mol)
Bisphosphonate	expt	FPPS−**risedronate**−IPP	*E. coli*		17.9	13.9	15.9	4.0	
		FPPS−**risedronate**−IPP	*T. brucei*		18.0	14.0	16.0	4.0	
		FPPS−**zoledronate**−IPP	*T. brucei*		14.9	10.9	12.9	4.0	
		FPPS−**11**−IPP	*T. brucei*		19.2	10.6	14.9	8.6	
	calcd	FPPS−**risedronate**−IPP							
		risedronate	*E. coli*	1RQJ	61.6	57.8	59.7	3.8	
		risedronate[e]	*E. coli*	1RQJ optimized	17.2	15.2	16.2	2.0	
IPP	expt	FPPS−risedronate−**IPP**	*E. coli*		−5.5	−9.2	−7.4	3.7	
		FPPS−zoledronate−**IPP**	*T. brucei*		−3.4	−10.2	−6.8	6.8	
		FPPS−11−**IPP**	*T. brucei*		−3.6	−10.2	−6.9	6.6	
	calcd	FPPS−risedronate−**IPP**							
		fully deprotonated **IPP**	*E. coli*	1RQJ	−2.6	−5.8	−4.2	3.2	
		fully deprotonated **IPP**[f]	*E. coli*	1RQJ optimized	0.2	11.5	5.9	11.3	
		monoprotonated **IPP**[g]	*E. coli*	1RQJ	−0.8	−5.6	−3.2	4.8	53.9
		monoprotonated **IPP**[g]	*E. coli*	1RQJ optimized	−4.3	−6.5	−5.4	2.2	1.7
		monoprotonated **IPP**[h]	*E. coli*	1RQJ	−2.2	−6.3	−4.3	4.1	39.7
		monoprotonated **IPP**[h]	*E. coli*	1RQJ optimized	−5.3	−11.5	−8.4	6.2	0.0
		monoprotonated **IPP**[i]	*E. coli*	1RQJ	−2.0	−4.3	−3.2	2.3	57.8
		monoprotonated **IPP**[i]	*E. coli*	1RQJ optimized	−1.1	−10.0	−5.6	8.9	3.0

[a] The predicted shifts are calculated by using the theory versus experiment relationship obtained in the text (eq 4). Bolded entries indicate sites of interest. [b] Tentative assignments are as follows: in risedronate, P1 and P2 are the phosphorus atoms coordinated with three and two Mg^{2+}, respectively; in IPP, P1 and P2 are the bridge and terminal phosphorus atoms, respectively. [c] $\delta_{av} = (\delta(P1) + \delta(P2))/2$; $|\Delta\delta| = |\delta(P1) - \delta(P2)|$. [d] The energy is referenced to that of the partially optimized structure of the system monoprotonated at O14 (taken to be 0). [e] Coordinates of the partially optimized structure are given in Table S10. [f] Coordinates of the partially optimized structure are given in Table S12. [g] The proton is added on the IPP terminal oxygen atom O13 (numbering in PDB file 1RQJ), which has a hydrogen bond with the neighboring Lys residue through nitrogen N^{ζ}. Coordinates of the partially optimized structure are given in Table S13. [h] The proton is added on the IPP terminal oxygen atom O14 (numbering in PDB file 1RQJ), which has a hydrogen bond with the neighboring Arg residue through nitrogen N^{ϵ}. Coordinates of the partially optimized structure are given in Table S14. [i] The proton is added on the IPP terminal oxygen atom O12 (numbering in PDB file 1RQJ), which has a hydrogen bond with the neighboring Arg residue through nitrogen NH_2. Coordinates of the partially optimized structure are given in Table S15.

solution[69] and do not imply any strong metal interactions—a result expected on the basis of the X-ray structures in which the IPP phosphates bind primarily to Arg and Lys residues. But what are the protonation states? For the bridging phosphate there are, in principle, four different protonation states (since the two oxygens are nonequivalent), and for the terminal phosphate there are 12 (3×2^2, since the three oxygens are nonequivalent: one is a P═O and the other two can be variously protonated), for a total of 48 states. However, many of these seem energetically unlikely, so we focused on the three dianions (containing a terminal monoanionic moiety), the form expected to predominate at pH = 7 in solution and observed in the crystallographic structure of ADP,[70] in addition to the fully deprotonated species. Results with the fully deprotonated species (−2.6, −5.8 ppm) were in reasonable accord with experiment (−5.5, −9.2 ppm, Table 3) but degraded considerably on geometry optimization. The shifts of the three monoprotonated species were all reasonably close to those seen experimentally (i.e., much better than the initial bisphosphonate shift predictions), and in the case of protonation on O14 (in PDB file 1RQJ), the computed shifts with the optimized structure (−5.3, −11.5 ppm) were very close to experiment and showed clear hydrogen-bond interactions with Arg117. The same conclusion (that O14 is protonated) is obtained when mean shift and absolute shift differences (between the two ^{31}P sites) are examined (Table 3), plus protonation on O14 resulted in the lowest energy structure (Table 3). When taken together, our results show that geometry optimization leads to bisphosphonate and IPP P−O bond lengths which are very close to those found in model systems (Figure S2), that the ^{31}P shifts are predicted with an average error of ~1.1 ppm (17.9/17.2, 13.9/15.2, −5.5/−5.3, and −9.2/−11.5 for the four experimental/theory data sets), and that the shifts of the lowest energy IPP species (the dianion protonated on O14) are in very good accord with the experimental shifts.

Crystallographic, Docking, and Mechanistic Implications. Given the results described above, we can begin to investigate how they might be used to suggest possible explanations for the activities of various bisphosphonates. For example, the addition of a side-chain CH_2 group to **2** to form **10** (homorisedronate) results in abrogation of activity, but addition of a side-chain CH_2 group to **9** (to form **11**) has no effect on activity. One possible explanation for this effect is that the more extended structure of **11** might result in a bound (*cis*-amidinium) conformation with a charge distribution closely resembling that of the most active bisphosphonates, zoledronate (**3**) and minodronate (**12**), as shown below:

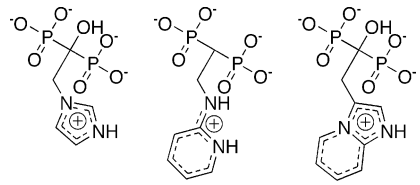

3 **11** **12**

To test this idea, we next solved the crystal structure of a minodronate (**12**)−*T. brucei* FPPS complex. We obtained data to 2.5 Å resolution and determined the structure (PDB ID 2EWG) shown in Figure 7A. The minodronate can be readily detected in the electron-density map, as shown in Figure 7B. Data collection and refinement statistics are shown in Table 4. When compared with the *T. cruzi* structure, there is a 0.94 Å rmsd between the two C^{α} backbones. This reduces to 0.81 Å if the loop and nine flanking residues are omitted. On the basis

(69) Song, Y. C.; Zhang, Y. H.; Wang, H.; Raker, A. M.; Sanders, J. M.; Broderick, E.; Clark, A.; Morita, C. T.; Oldfield, E. *Bioorg. Med. Chem. Lett.* **2004**, *14*, 4471−4477.
(70) Cini, R.; Pifferi, C. *J. Chem. Soc., Dalton Trans.* **1999**, 699−710.

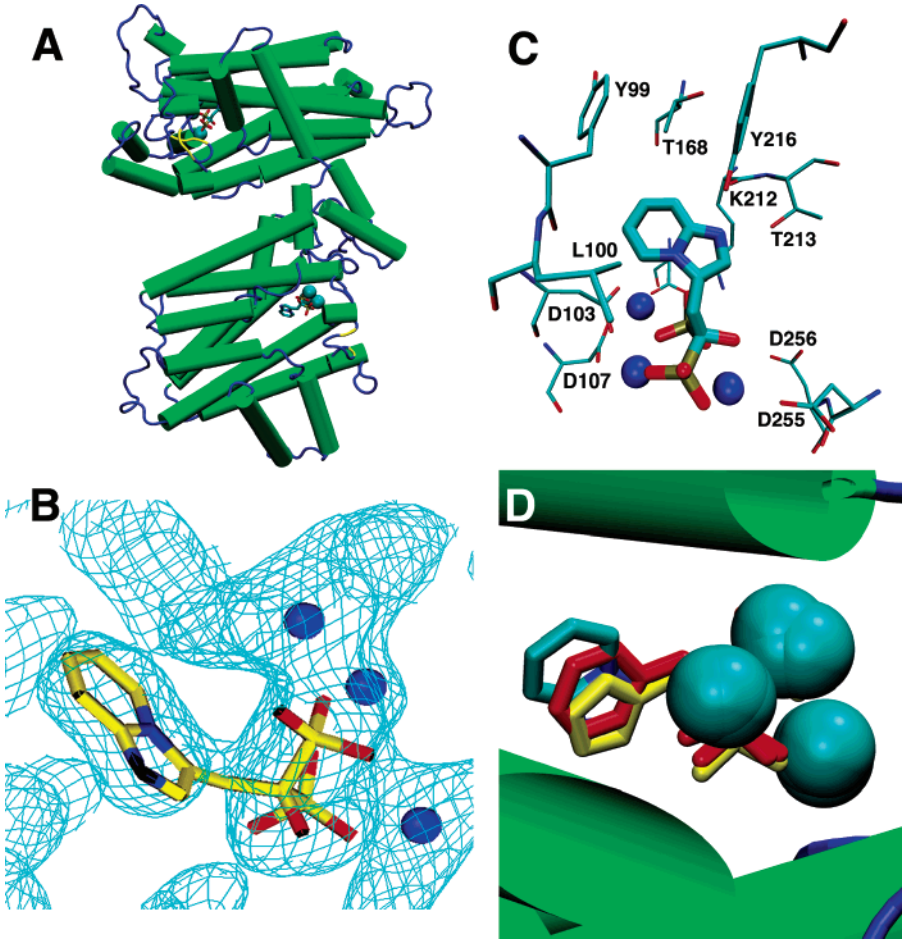

Figure 7. X-ray crystallographic results for minodronate/FPPS. (A) Whole protein view of *T. brucei* FPPS/minodronate/Mg^{2+} complex. (B) Electron density of minodronate and three Mg^{2+} ions (contoured at 1.2σ in the $2F_o - F_c$ map). (C) Minodronate-protein contacts in active site. (D) Alignment of minodronate, risedronate (red, from human FPPS, PDB ID 1YV5), and zoledronate (yellow, from human FPPS, PDB ID 1ZW5). Alignments were created by using the "align-by-homology" function in Sybyl 7.1 to align the protein C^{α} atoms. Figure parts A and D were prepared using the VMD program (ref 74).

of the entire sequences, an rmsd of ~0.74 Å might be expected from the empirical correlation of Chothia and Lesk.[71] The slight deviations could be due to inadequacies in our refinement, although of course it should be noted that the minodronate structure here does not contain IPP, which has been shown to cause a "closing" of the ternary complex structure, at least in human FPPS.[28]

Minodronate in the *T. brucei* FPPS structure binds and has protein contacts (e.g., the two DD repeats interacting with the Mg_3-bisphosphonate fragment, Figure 7C) similar to those seen in other bisphosphonate−FPPS structures (risedronate/*E. coli*, alendronate/*S. aureus*, risedronate/*H. sapiens*, zoledronate/*H. sapiens*, risedronate/*T. brucei*, and risedronate/*T. cruzi*), independent of whether the homoallylic (IPP) binding site is occupied or not. In particular, we find that the two minodronate phosphonate groups bind to three Mg^{2+}, as shown in Figure 7D. This bisphosphonate−Mg_3^{2+} motif is present in a broad range of eukaryotic as well as prokaryotic bisphosphonate−FPPS complexes[26−29] and is unaffected by either occupation of the IPP site or the size of the bisphosphonate side chain. Two of these Mg^{2+} form rather symmetric six-membered rings with the bisphosphonate acting as a bidentate chelate, while the third Mg^{2+} is involved in additional interactions with P2. This can

(71) Chothia, C.; Lesk, A. M. *EMBO J.* **1986**, *5*, 823−826.

Table 4. Data Collection and Refinement Statistics for *T. brucei* FPPS Complexed with Minodronate

space group	*C*2
unit-cell parameters	
a, *b*, *c* (Å)	131.98, 118.10, 63.25
β (°)	112.48
	Data Collection Statistics
X-ray source	BNL-X12C
wavelength (Å)	1.1
resolution (Å)	30−2.50 (2.59−2.50)
total reflections	102 498
unique reflections	30 546
Completeness (%)	96.5 (79.4)
R_{merge} (%)	6.9 (35.6)
average I/σ (I)	28.2 (3.3)
multiplicity	3.4
	Refinement Statistics
R_{all} (%)	24.10
R_{work} (%)	24.24
R_{free} (%)	25.98
rms bond lengths (Å)	0.004
rms bond angles (°)	1.435
total atoms of protein	5876
ligand	2 minodronates
solvent (water)	330
metals	6 Mg^{2+}
$B_{average}$ (Å^2)	33.24 (main and protein side-chain atoms) 31.90 (minodronate and Mg^{2+})

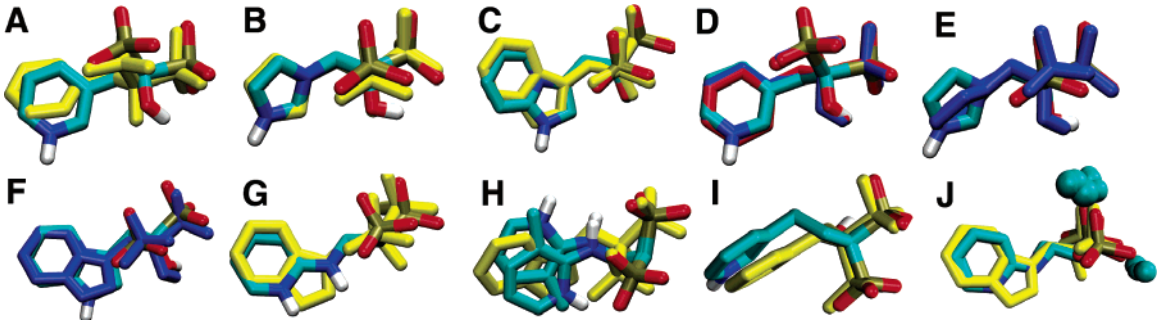

Figure 8. Computational docking results. Shown are the best docked results for (A) protonated risedronate (colored by atom type) docked to human FPPS (PDB ID 1YV5), compared with the crystallographic structure (yellow); (B) protonated zoledronate (colored by atom type) docked to human FPPS (PDB ID 1ZW5), compared with the crystallographic structure (yellow); (C) protonated minodronate (colored by atom type) docked to human FPPS (PDB ID 1YV5), compared with the *T. brucei* FPPS structure (yellow); (D) protonated risedronate (colored by atom type), deprotonated risedronate (blue), and **21** (red) docked to human FPPS (PDB ID 1YV5); (E) protonated zoledronate (colored by atom type) and deprotonated zoledronate (blue) docked to human FPPS (PDB ID 1ZW5); (F) protonated minodronate (colored by atom type) and deprotonated minodronate (blue) docked to human FPPS (PDB ID 1YV5); (G) protonated *cis*-**11** (colored by atom type) docked to human FPPS (PDB ID 1YV5), compared with the X-ray structure of minodronate (yellow); (H) protonated *cis*- and *trans*-**22** (colored by atom type) docked to human FPPS (PDB ID 1YV5), compared with the X-ray structure of minodronate (yellow); (I) protonated **10** (colored by atom type) docked to human FPPS (PDB ID 1YV5), compared with the X-ray structure of risedronate (yellow). (J) Comparison between **11** (blue) and **12** (yellow)−FPPS X-ray structures. Alignments were created by using the "align-by-homology" function in Sybyl 7.1 to align the protein C^{α} atoms. Figure was prepared by using the VMD program (ref 74).

be clearly seen in Figure 7D, in which we superimpose the minodronate structure on those reported previously for the single-ring species risedronate (**2**) and zoledronate (**3**). The structures were all aligned by using the C^{α} backbone coordinates of the *T. cruzi*, *T. brucei*, and *H. sapiens* proteins (Sybyl 7.0 Program[64]), so some differences in bisphosphonate and Mg^{2+} positions are expected, given the considerable sequence differences with the human protein, but clearly the phosphonate groups, the Mg^{2+}, and the overall side-chain conformations are all very similar, with the five-membered rings of minodronate and zoledronate having only a 0.56 Å rmsd (Figure 7D).

Since crystallographic structures are not always available, we next investigated to what extent these structures could be reproduced by using Autodock, employing the backbone (−4) and side-chain (+1) charges determined from the NMR and QM calculations described above, a prelude to using docking to try to probe some of the puzzling structure−activity results described in the Introduction. This work extends that reported previously for risedronate, and, as may be seen in Figure 8A−C, we find very good accord between the computational and experimental results for the protonated forms of risedronate, zoledronate, and minodronate. For risedronate docking to the *E. coli* FPPS (PDB ID 1RQJ), there is a 0.38 Å rmsd between the crystallographic and computational results, while for docking risedronate and zoledronate to the human FPPS (PDB IDs 1YV5 and 1ZW5) we obtain rmsds of 0.80 and 0.55 Å, respectively. For minodronate, docking to the best human FPPS structure (PDB ID 1YV5, 2.0 Å resolution) gave a 0.47 Å deviation versus the *T. brucei* minodronate X-ray structure (Figure 8C).

While these results are of interest, they do not specifically address the possible importance of the +1 side-chain charge. We thus next investigated the docking of the free base forms of **2**, **3**, and **12**. All compounds docked in essentially the same pose (Figure 8D−F); however, the docking energies were uniformly more negative (favorable) for each of the three protonated side-chain-containing species: −24.93, −23.70 kcal (risedronate); −26.60, −25.94 kcal (zoledronate); and −25.37, −24.41 kcal (minodronate). Also, the docking pose for the deaza (or phenyl) analogue of risedronate (**21**) was essentially the same as that for the non-protonated form of risedronate (Figure 8D),

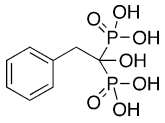

21

as were the binding energies (−23.70 and −23.81 kcal for deprotonated risedronate and **21**, respectively). These results indicate that (1) the docking poses for each compound are quite well predicted, independent of charge state, but (2) the binding energies of the protonated species are all uniformly more negative, consistent with the idea that it is the positively charged species that bind more favorably into the FPPS active site.

We next carried out a docking calculation for **11** (in its protonated form), the species whose activity is much higher than that of homorisedronate (**10**). The amidinium group in **11** is expected to be planar since, as shown in Table S16 (Supporting Information), there is a large (∼14 kcal) barrier to rotation, a result in agreement with a recent NMR study of related compounds.[72] Table S16 also shows computed ^{15}N NMR chemical shift differences ($\Delta\delta = \delta^{15}N^{\gamma} - \delta^{15}N^{\epsilon}$): the *cis* and *trans* $\Delta\delta$ values (60.3, 56.0 ppm) are those closest to experiment (58.2 ppm), so we constrained χ_2 in the docking calculations to 0° and 180°. The final docked energy was marginally lower for the *cis* species, but the overall poses were quite similar. More interestingly, the docked pose for *cis*-**11** was virtually superimposable with the experimental result obtained for minodronate, as shown in Figure 8G. This suggests an explanation for the unexpectedly high potency of **11**, since its docked structure would place positive charge density in the region where positive charge would be expected in minodronate (or in zoledronate). The dipoles of several oxygen atoms in the FPPS active site (in the *T. brucei* enzyme, these are the carbonyl oxygen of Lys212, the side-chain oxygen of Thr213, and the carbonyl oxygen of Gln252) likely stabilize the carbocation charge, and the results of an electrostatic potential calculation for *T. brucei* FPPS using a linearized Poisson−Boltzmann equation (the Molcad module in Sybyl 7.0[58]) shown in Figure

(72) Matczak-Jon, E.; Slepokura, K.; Kafarski, P. *J. Mol. Struct.* **2006**,*782*, 81−93.

S5 (Supporting Information) support this idea. The blue region near the minodronate NH represents a relatively negative electrostatic potential, which would interact favorably with the charged minodronate side chain (and other positively charged bisphosphonate side chains as well) but would not interact favorably with uncharged side chains. These docking results thus support the idea that the most potent, nitrogen-containing bisphosphonates bind to FPPS in their protonated forms and that the carbocation side chains are stabilized in the active site by electrostatic complementarity.[73] The docking results also suggest why homorisedronate (**10**) is inactive while **11** (which also contains an extended side chain) is active, since the latter has extensive charge delocalization and can bind in a pose very similar to that seen with minodronate. In the case of **22** (which is inactive), the methyl analogue of **11**, both cis and trans forms

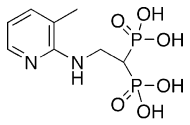

22

dock with a much poorer register with minodronate (Figure 8H). Likewise, the atoms in the aromatic ring in homorisedronate (**10**) have a 0.97 Å rms displacement from the plane formed by the ring of risedronate (Figure 8I). So, in all cases where structures are known, the docking results reproduce the crystallographic results, and the docking energies are more favorable for the protonated side-chain-containing species. The active, extended amidinium side-chain species **11** docks in essentially the same way as does minodronate, while the much less active methyl analogue (**22**), as well as the inactive species homorisedronate (**10**), clearly has much worse register with the active-site species minodronate and/or risedronate, giving a likely explanation for the structure−activity relationships seen experimentally.

Finally, after completion of this work, we succeeded in obtaining crystals of a *T. brucei* FPPS−**11** complex and determined its structure, as described for the minodronate−FPPS structure. Data collection statistics are given in the Supporting Information (Table S10). The structure obtained is very similar to that seen with minodronate (superimposition of **11**, **12**, and Mg^{2+} bonded to FPPS shown in Figure 8J) and is very close (0.99 Å, heavy atom rmsd) to that predicted by the docking calculations, strongly supporting the validity of the latter.

Conclusions

The results we have presented herein are of interest for several reasons. First, we have used solid-state ^{13}C and ^{15}N NMR to answer the question of the protonation states of the side chain of the nitrogen-containing bisphosphonates used in treating various bone resorption diseases. These bisphosphonates bind to their farnesyl diphosphate synthase target as protonated side-chain (pyridinium, imidazolium, alkylammonium, or amidinium)-containing species. Second, we determined the crystallographic structures and solid-state ^{31}P NMR spectra of a series of bisphosphonates and used QM methods to analyze the results obtained. There was a good correlation between theory and experiment: in almost all cases, the anionic or deprotonated groups were more shielded. Third, we applied these same methods to investigate bisphosphonate backbone binding to the FPPS active site. There was a remarkable similarity in the shifts for risedronate bound to both the *E. coli* and *T. brucei* FPPS and the IPP shifts in a series of *E. coli* FPPS−bisphosphonate complexes. In the *E. coli* FPPS−risedronate−IPP complex, the protein crystal structure did not permit successful prediction of the bisphosphonate shifts, but use of geometry-optimized structures did and indicated the presence of a fully deprotonated bisphosphonate backbone (consistent with multiple PO_3-Mg^{2+} interactions). Fourth, we used QM methods to deduce the protonation state of the IPP ligand: the shifts observed suggest the presence of a dianionic diphosphate, protonated on the terminal phosphate group. Fifth, we report the first crystal structure of the potent bicyclic bisphosphonate, minodronate (**12**), bound to FPPS. Sixth, we used computational docking methods, combined with knowledge obtained from the NMR, QM, and X-ray investigations, to suggest a structural basis for the unusual activity of some bisphosphonates, and the lack of activity of others, on the basis of known and predicted active-site conformations. And seventh, we obtained the X-ray structure of the potent aminopyridyl bisphosphonate **11** bound to *T. brucei* FPPS, finding good accord with the structure predicted computationally. Overall, these results are of general interest since they show how using NMR, crystallographic, quantum chemical, and computational docking techniques in combination can provide new insights into the binding of an important class of drug molecules, bisphosphonates, to their protein target, opening the way for the design of other, more potent and/or selective inhibitors of FPPS, and potentially of other isoprene biosynthesis pathway enzymes as well.

Acknowledgment. This work was supported by the United States Public Health Service (NIH grant GM-65307). J.M., S.M., and J.M.S. were supported by Predoctoral Fellowship Awards from the American Heart Association, Greater Midwest Affiliate. Y.S. was supported by a Leukemia and Lymphoma Society Special Fellowship. Y.Z. was supported by an American Heart Association, Greater Midwest Affiliate, Postdoctoral Fellowship. G.A.M. was supported by an NIH Ruth L. Kirschstein NRSA Postdoctoral Fellowship (grant GM-65782). We are grateful to Chad Rienstra and Scott Wilson for their helpful advice; to Novartis Pharma AG, Basel, for providing several bisphosphonates; and to David Hosfield (Takeda San Diego, Inc., San Diego, CA) for providing the *E. coli* FPPS expression system.

Supporting Information Available: Complete refs 45 and 46, and additional crystallographic and computational data (PDF, CIF). This material is available free of charge via the Internet at http://pubs.acs.org.

JA061737C

(73) McCoy, A. J.; Epa, V. C.; Colman, P. M. *J. Mol. Biol.* **1997**, *268*, 570−584.
(74) Humphrey, W.; Dalke, A.; Schulten, K. *J. Mol. Graph.* **1996**, *14*, 33−38.